



Interannual variability of surface air temperature over mid-high latitudes of Eurasia during boreal autumn

Shangfeng Chen¹ · Renguang Wu^{1,3,4} · Linye Song² · Wen Chen^{1,3}

Received: 10 November 2018 / Accepted: 18 March 2019 / Published online: 22 March 2019
© Springer-Verlag GmbH Germany, part of Springer Nature 2019

Abstract

This study analyzes the dominant modes of interannual variability of surface air temperature (SAT) during boreal autumn over the mid-high latitudes of Eurasia and investigates their associations with snow cover, atmospheric circulation and sea surface temperature (SST). The first, second and third empirical orthogonal function (EOF) mode of autumn SAT anomalies displays same-sign distribution, an east–west dipole pattern and a south–north dipole pattern, respectively. Analysis of surface heat fluxes indicates that snow changes explain only small patches of SAT anomalies related to the first two EOFs via altering surface shortwave radiation. Atmospheric circulation anomalies have important contributions to the formation of SAT anomalies. Southerly (northerly) wind anomalies generally favor positive (negative) SAT anomalies via bringing warmer (colder) air from lower (higher) latitudes. The atmospheric circulation anomalies related to the first EOF mode are attributed to a combination of the Arctic Oscillation (AO) and the Scandinavia pattern and those related to the second EOF mode have a close relation with the East Atlantic/West Russian (EAWR) and circumglobal teleconnection (CGT) patterns. Formation of the atmospheric circulation anomalies related to the third EOF mode is partly related to the Arctic sea ice change around the Barents–Kara Seas. SST anomalies have little contribution to the atmospheric circulation anomalies associated with the first three EOF modes of Eurasian autumn SAT interannual variations. Hindcast skill of the SAT anomalies related to the first (second) EOF mode is improved when taking both the AO and Scandinavia (EAWR and CGT) patterns into account.

Keywords Surface air temperature · Boreal autumn · Atmospheric teleconnection pattern · Snow · Arctic sea ice

1 Introduction

Surface air temperature (SAT) is one of the most important variables in global climate variability and change (IPCC 2013). Changes in SAT may exert considerable influences on climate, ecosystem, marine, fisheries, crop growth, and

human health (Yao 1995; Stott et al. 2004; Feudale and Shukla 2010; Ye et al. 2013; Caloiero 2017). For example, the crop yield over northeastern China was notably sensitive to local SAT change (Yao 1995). The high SAT and the accompanying strong heat waves over Europe in summer of 2003 led to extensive forest fire and resulted in considerable human death and economic loss (Stott et al. 2004; Feudale and Shukla 2010). The extremely cold winter during 2009 and the extremely warm summer during 2010 over most parts of the Eurasia had substantial impacts on agriculture, fishery, electricity supply and people's daily activity (Barriopedro et al. 2011; Matsueda 2011; Otomi et al. 2013). Studies demonstrated that SAT anomalies can modulate the soil moisture and subsequently alter the energy exchange between the low-level atmosphere and land and lead to change in the overlying atmospheric circulation (Henderson-Sellers 1996; Labat et al. 2004). SAT variations over Eurasia also have a significant modulation on the Asian monsoon activity via changing the thermal contrast between the Eurasian continent and surrounding oceans (e.g. Lau and Li

✉ Renguang Wu
renguang@mail.iap.ac.cn

¹ Center for Monsoon System Research, Institute of Atmospheric Physics, Chinese Academy of Sciences, Beijing 100029, China

² Institute of Urban Meteorology, China Meteorological Administration, Beijing, China

³ State Key Laboratory of Numerical Modeling for Atmospheric Sciences and Geophysical Fluid Dynamics, Institute of Atmospheric Physics, Chinese Academy of Sciences, Beijing, China

⁴ School of Earth Sciences, Zhejiang University, Hangzhou, China

1984; Liu and Yanai 2001; D'Arrigo et al. 2006). Due to substantial impacts of Eurasian SAT variations, it is important to identify the dominant modes of Eurasian SAT variability and unravel the factors and the underlying processes.

Several previous studies have examined spatial patterns of the SAT interannual variability over Eurasia during boreal winter and spring. Miyazaki and Yasunari (2008) demonstrated that the first empirical orthogonal function (EOF) mode of winter SAT variability over Asia and the surrounding oceans displays a north–south dipole pattern and has a close relation with the Arctic Oscillation (AO). Chen et al. (2016b) revealed that the first EOF of spring SAT variations over Eurasia displays consistent anomalies, and the spring AO-related atmospheric anomalies play important roles for SAT anomalies related to the first EOF. Several studies have examined the dominant modes of boreal summer SAT anomalies over Eurasia, albeit mainly focusing on sub-regions of Eurasia (e.g. Chen et al. 2016a). However, few studies have been conducted about the interannual variability of boreal autumn SAT over the mid-high latitudes of Eurasia. Hence, one goal of the current study is to identify the leading modes of interannual variability of boreal autumn SAT over the mid-high latitudes of Eurasia. Understanding the autumn SAT variations over Eurasia is important for improving knowledge of related surface condition (e.g. snow cover) changes that may influence following winter climate (Jhun and Lee 2004; Wang et al. 2010; Luo and Wang 2018; King et al. 2018).

Interannual variations of Eurasian SAT are impacted by several factors, such as sea surface temperature (SST) (Wu et al. 2009, 2011; Wu and Chen 2016), Arctic sea ice (Liu et al. 2012; Cohen et al. 2012, 2014; Chen et al. 2014; Sun et al. 2016; Chen and Wu 2018; Chen and Song 2018), Eurasian snow cover (Ye et al. 2015; Chen et al. 2016b), and atmospheric circulation patterns (Thompson and Wallace 2000; Gong et al. 2001; Wu and Wang 2002; Cheung et al. 2012; Cheung and Zhou 2015; Otomi et al. 2013; Park and Ahn 2016). Wu et al. (2011) and Chen et al. (2016b) indicated that spring North Atlantic SST anomalies may induce an atmospheric wave train propagating from the North Atlantic to Eurasia. The resultant atmospheric circulation anomalies further lead to Eurasian SAT changes during boreal spring and summer. Studies indicated that Eurasian snow cover changes during boreal winter and spring have a contribution to the interannual variation of SAT anomalies via modulating surface shortwave radiation (Ye et al. 2015; Chen et al. 2016b; Wu and Chen 2016). The preceding autumn Arctic sea ice change may contribute to the following Eurasian winter and spring SAT change (Wu et al. 2011; Chen et al. 2014; Sun et al. 2016).

Previous studies showed that the atmospheric teleconnection patterns, such as the AO, North Atlantic Oscillation (NAO), western Pacific (WP), Pacific North American

(PNA), East Atlantic (EA), East Atlantic/Western Russia (EAWR), and Scandinavia (SCAND) teleconnection patterns, etc., may have a significant impact on the Eurasian SAT anomalies (Barnston and Livezey 1987; Chen et al. 2016b, 2018a). In particular, AO is the leading EOF pattern of interannual variability of atmospheric anomalies over extratropical Northern Hemisphere (NH) (Thompson and Wallace 2000). The NAO is the first EOF pattern of atmospheric variability over the North Atlantic Ocean (Hurrell and van Loon 1997). It may be a regional manifestation of the AO over the North Atlantic Ocean and the AO includes most of the features related to the NAO (Thompson and Wallace 2000). The PNA is an important pattern of the atmospheric variability over the North Pacific–North American regions (Wallace and Gutzler 1981; Barnston and Livezey 1987). The WP pattern is a south–north dipole mode with one center of anomalies over the subtropical western North Pacific and the other center of opposite sign over the Kamchatka Peninsula (Linkin and Nigam 2008). The EA pattern is another mode of the North Atlantic atmospheric variability (Barnston and Livezey 1987). The EAWR pattern has four primary centers, with same-sign geopotential height anomalies over Europe and north China, and geopotential height anomalies with opposite sign over the central North Atlantic and north of the Caspian Sea (Barnston and Livezey 1987). Furthermore, the SCAND pattern has a dominant center of anomalies around the Scandinavia and weaker anomalies of opposite sign over the eastern Russian–western Mongolia and west Europe (Barnston and Livezey 1987).

At present, it is still unclear what are the main factors contributing to interannual variability of boreal autumn SAT over the mid-high latitudes of Eurasia. Hence, the second goal of this study is to examine the factors for the Eurasia SAT variations during boreal autumn and the underlying physical processes. This may help to understand the source of predictability of SAT variations over the mid-high latitudes of Eurasia. The structure of this paper is as follows. Section 2 describes the data and methods. Section 3 analyzes the dominant modes of the Eurasian autumn SAT interannual variation. Section 4 investigates the possible roles of snow cover change in the SAT anomalies via analysis of surface heat fluxes. Section 5 examines roles of SST, atmospheric circulation and Arctic sea ice anomalies in the interannual variation of Eurasian autumn SAT. Section 6 provides a summary.

2 Data and methods

The present study employs monthly mean geopotential height, horizontal winds, total cloud cover (TCC), surface winds, surface longwave and shortwave radiations, surface latent and sensible heat fluxes from the National Centers for Environmental

Prediction-National Center for Atmospheric Research (NCEP-NCAR) reanalysis (Kalnay et al. 1996; <ftp://ftp.cdc.noaa.gov/Datasets/ncep.reanalysis.derived/>). The NCEP-NCAR reanalysis data are available from 1948 to the present. Geopotential height and horizontal winds at pressure levels are on 2.5° latitude-longitude grids. Surface winds, TCC, and surface heat fluxes are on T62 Gaussian grids.

The monthly mean SAT data are extracted from the University of Delaware from 1900 to 2014, which have a horizontal resolution of $0.5^\circ \times 0.5^\circ$ (Matsuura and Willmott 2009; <https://www.esrl.noaa.gov/psd/data/gridded/>). This study employs monthly mean SST from the National Oceanic and Atmospheric Administration (NOAA) Extended Reconstructed SST, version 3b (Smith et al. 2008; <http://www.esrl.noaa.gov/psd/data/gridded/>). The ERSSTv3b SST data are available from 1854 to the present and have a horizontal resolution of $2^\circ \times 2^\circ$. Monthly sea ice concentration (SIC) data are obtained from the Hadley Centre Sea Ice and Sea Surface Temperature dataset (HadISST) (Rayner et al. 2003; <http://www.metoffice.gov.uk/hadobs/hadisst>). The HadISST SIC data have a resolution of $1^\circ \times 1^\circ$ and are available from 1870 to the present. The present study also uses the boreal autumn (September–October–November-averaged, SON) mean snow cover extent (SCE) data from the Northern Hemisphere 25 km Equal-Area Scalable Earth Grid (EASE-Grid) weekly Snow Cover and Sea Ice Extent, version 3, product (Brodzik and Armstrong 2013; <ftp://sidads.colorado.edu/pub/DATASETS>). The raw weekly SCE has been converted to monthly mean on a regular horizontal resolution of $1^\circ \times 1^\circ$. The EASE-Grid SCE data are available after October 1966. The monthly mean snow depth (SD) data since 1979 was obtained from the ERA-Interim with a horizontal resolution of $1^\circ \times 1^\circ$ (Dee et al. 2011; available at Website of <http://apps.ecmwf.int/datasets/>).

Climate indices of AO, NAO, WP, PNA, EA, EAWR, and SCAND are provided by the National Oceanic and Atmospheric Administration (NOAA) Climate Prediction Center (CPC) (<https://www.esrl.noaa.gov/psd/data/climateindices/>). These climate indices are available from 1950 to the present. As in Ding and Wang (2005), CGT index is calculated as the region-averaged 200 hPa geopotential height anomalies over $35^\circ\text{--}40^\circ\text{N}$ and $60^\circ\text{--}70^\circ\text{E}$. This study employed the stationary wave activity flux (WAF) in Takaya and Nakamura (2001) to describe propagation of atmospheric stationary Rossby wave. Equation of the WAF is written as follows (Takaya and Nakamura et al. 2001):

$$W = \frac{p}{2|\vec{U}|} \left\{ \begin{array}{l} U(v'^2 - \psi' v'_x) + V(-u' v' + \psi' u'_x) \\ U(-u' v' + \psi' u'_x) + V(u'^2 + \psi' u'_y) \\ \frac{f_o R_a}{N^2 H_o} [U(v' T' - \psi' T'_x) + V(-u' T' - \psi' T'_y)] \end{array} \right\},$$

where $\vec{U} = (U, V)$, ψ' , and $\vec{V}' = (u', v')$ represent the mean winds, perturbed geostrophic stream function and winds,

respectively. N , f_o , T' , H_o , R_a , and p denote the Brunt–Vaisala frequency, the Coriolis parameter at 45°N , perturbed air temperature, the scale height, gas constant related to the dry air, and pressure normalized by 1000 hPa, respectively. The subscript x (y) denotes derivative in the zonal (meridional) direction. Climatological means are calculated based on the period over 1950–2014. Perturbed geostrophic stream function and winds correspond to the anomalies obtained by regression against an involved time series.

Statistically significance levels of the correlation and regression coefficients are estimated based on the two-tailed Student's t test. This study focuses on analyzing the variations on the interannual timescales. Hence, all the original variables and indices are subjected to a 9-year high pass Lanczos filter to obtain their interannual components (Duchon 1979). We have calculated the percent of SAT variance explained by the interannual variability during autumn over the mid-high latitudes of Eurasia (Fig. 1). The percent variance is above 60% over most parts of Eurasia north of 40°N (Fig. 1).

3 Dominant patterns of boreal autumn SAT anomalies

We extract the dominant patterns of boreal autumn (SON) SAT anomalies over the mid-high latitudes of Eurasia ($40^\circ\text{--}70^\circ\text{N}$ and $0^\circ\text{--}140^\circ\text{E}$) via the EOF analysis method. SAT anomaly fields are weighted by the cosine of the latitude to account for decrease of the area with the increase in the latitude (North et al. 1982a). The first three EOF modes explain 43.7%, 16.3%, and 12.6% of the total variance, respectively. These EOF modes are well separated from each other and from the other EOF modes according to the method of North et al. (1982b). This study focuses on

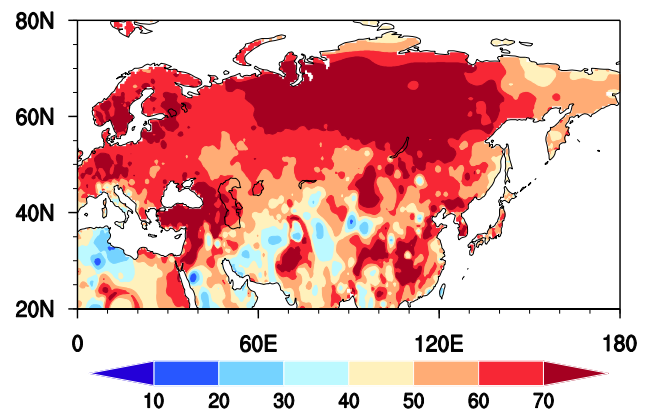


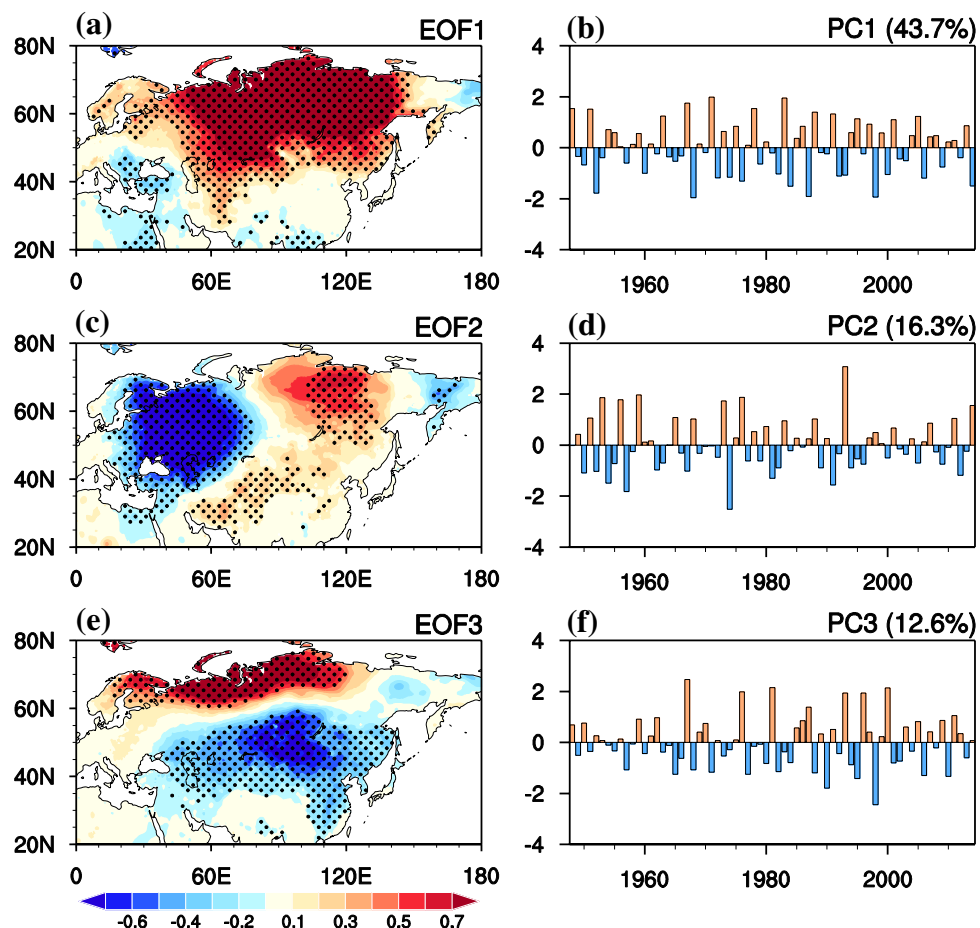
Fig. 1 Percentage of variance of the boreal autumn (SON) SAT variation over the mid-high latitudes of Eurasia explained by its interannual component during 1948–2014. Unit is %

analyzing the first three EOF modes (i.e., EOF1, EOF2, and EOF3) as the percentage variances of other EOF modes are relatively small.

The EOF1 is featured by same-sign SAT anomalies over most parts of the mid-high latitudes of Eurasia (north of 40°N), with a maximum center around the central Siberia (Fig. 2a). Opposite SAT anomalies with much smaller amplitude are seen around the Balkan Peninsula (Fig. 2a). The EOF2 is characterized by an east–west dipole pattern, with one center of SAT anomalies over the East European Plain and the other center of opposite sign north of the Lake Baikal (Fig. 2c). The EOF3 is featured by a meridional dipole pattern, with large SAT anomalies over the north coast of the Eurasia between 20°E and 120°E and opposite sign SAT anomalies around $30^{\circ}\text{--}50^{\circ}\text{N}$ and $50^{\circ}\text{--}120^{\circ}\text{E}$ (Fig. 2e). The corresponding PC time series show clear interannual variations during 1948–2014 (Fig. 2b, d, f).

In the following sections, we analyze the factors responsible for the formation of the SAT anomalies related to the above three EOF modes. We first discuss contribution of the Eurasian snow cover change. Then, we examine roles of atmospheric circulation anomalies.

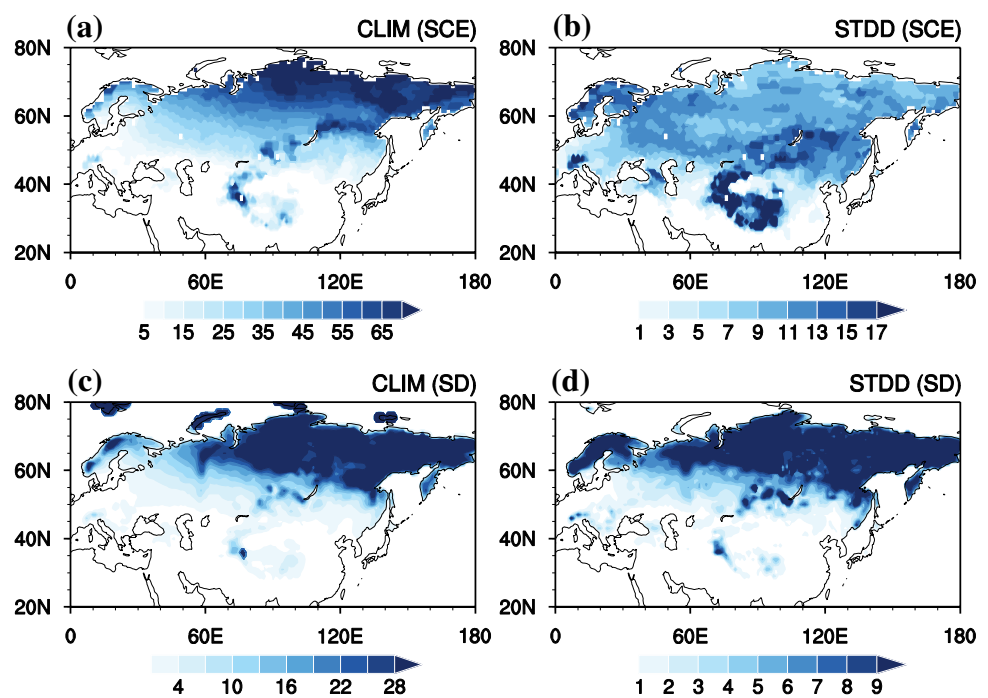
Fig. 2 Boreal autumn SAT (unit: $^{\circ}\text{C}$) anomalies obtained by regression against the standardized principal component (PC) time series corresponding to **a** EOF1, **c** EOF2, and **e** EOF3 of the SAT anomalies over Eurasian mid-high latitudes ($40^{\circ}\text{--}70^{\circ}\text{N}$, and $0^{\circ}\text{--}140^{\circ}\text{E}$) in boreal autumn during 1948–2014. **b**, **d**, and **f** are the corresponding standardized PC1, PC2, and PC3 time series. Stippling regions in **a**, **c**, **e** indicates SAT anomalies significant at the 95% confidence level based on the two tailed Student's *t* test



4 Roles of snow cover changes in the SAT anomalies

This section investigates the potential connection of autumn SAT anomalies with the snow changes. Studies have demonstrated that snow cover change can influence SAT anomalies via the snow-albedo effect and the snow hydrological effect (Barnett et al. 1989; Yasunari et al. 1991). For the snow-albedo effect, snow cover anomalies impact SAT through change in surface shortwave radiation (SWR) (Yasunari et al. 1991). The snow-hydrological effect involves consumption of heat for snow melting and increase in the moisture of the land surface after the snow melting (Yasunari et al. 1991). Before investigating connection of the autumn SAT anomalies with snow changes, we first examine the climatology and standard deviation of SCE and SD. Climatological mean SCE and SD display similar spatial distribution over Eurasia, with larger values over higher latitudes (Fig. 3a, c). Relatively large interannual variability of the autumn SCE is present over the Tibetan Plateau, north Europe, and East Siberia (Fig. 3b). For the SD, spatial distribution of the standard deviation (Fig. 3d) resembles well that of climatological

Fig. 3 Climatology of autumn
a SCE and **c** SD. Standard deviation of autumn **b** SCE and **d** SD. Unit is % for SCE and mm of water equivalent for SD.
a, c and **b, d** are constructed based on the period 1967–2014 and 1979–2014, respectively. Long-term linear trends of the SCE and SD are not removed in calculating their climatology mean and standard deviation



mean (Fig. 3c). The areas with larger climatological mean tend to have larger interannual variability of SD (Fig. 3c, d).

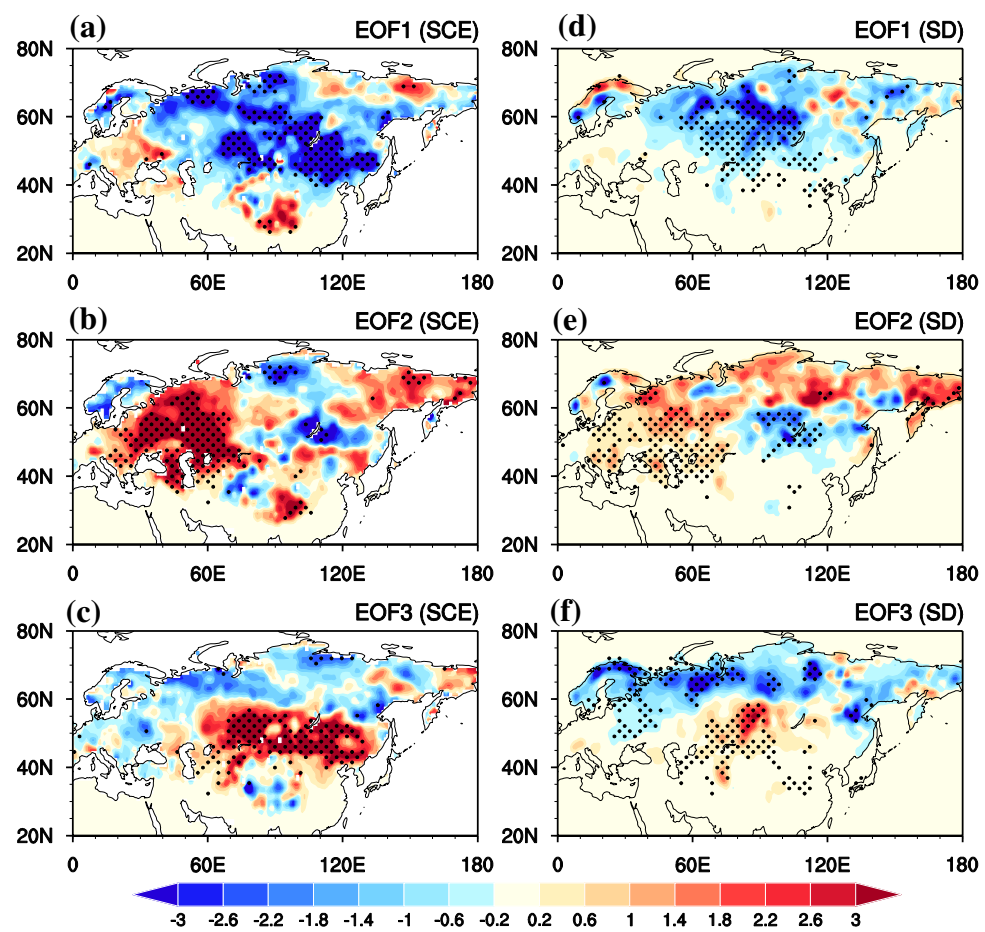
In the following, we further examined the SCE and SD anomalies associated with the first three EOF modes. To a large extent, spatial distributions of the autumn SCE anomalies related to the first three EOF modes over Eurasia (Fig. 4a–c) are similar to those of the SD anomalies (Fig. 4d–f) though the regions with significant SCE anomalies are slightly larger. For the first EOF mode, decreases in the SCE and SD anomalies are observed around 40°–70°N and 60°–120°E (Fig. 4a, d) corresponding to positive SAT anomalies there (Fig. 2a). This implies a possible contribution of the snow change to the SAT anomalies. This is because decrease in the snow cover may lead to decrease in surface albedo, which results in more SWR absorbed by the surface and contributes to SAT increase. For the second EOF mode, increases in SCE and SD are seen around the East European Plain and the Russian Far East (Fig. 4b, e) corresponding to negative SAT anomalies (Fig. 2c). In addition, negative SCE and SD anomalies are present around the Lake Baikal. For the third EOF mode, the SCE and SD anomalies display a south–north dipole pattern, with positive (negative) values south (north) of 45°N (Fig. 4c, f). The correspondence between the SAT and snow anomalies over several regions of Eurasia implies that formation of the SAT anomalies may be partly related to the snow cover change.

The snow and SAT changes may involve one way effect or two-way interactions. On one hand, snow anomalies may lead to SAT changes via the snow-hydrological effect and the snow-albedo effect (Barnett et al. 1989; Yasunari et al.

1991). On the other hand, SAT anomalies may lead to snow cover changes (Ye et al. 2015; Chen et al. 2016b). Increases (decreases) in SAT are favorable for consumption (accumulation) of snow. Hence, it is hard to separate the effect of snow on the SAT variation only through comparison of the spatial distributions of the SCE and SAT anomalies.

Following previous studies (Ye et al. 2015; Chen et al. 2016b), surface heat flux changes are examined to help understand the effect of the snow cover change on the SAT anomalies. The effect of snow cover changes on the SAT anomalies can be captured by surface heat flux anomalies (Barnett et al. 1989; Yasunari et al. 1991; Ye et al. 2015; Chen et al. 2016b). Specifically, snow cover anomalies may change surface heat fluxes in several ways. Snow changes affect SWR via modulating surface albedo. Decreases (increases) in snow cover result in more (less) SWR absorbed by the surface, which contributes to increases (decreases) in SAT (Ye et al. 2015; Chen et al. 2016b). Increase in snow amount leads to consumption of more heat energy for the snow melting. As a result, less heat energy is available to warm surface air, which results in SAT decrease. This process may be captured by surface sensible heat flux (SHF) change through the temperature contrast between the ground surface and surface air. It can also be captured by surface upward longwave radiation change (LWR) because change in LWR is related to surface temperature change. Specifically, increase in snow is associated with decrease in upward SHF because of the decrease in difference between the land surface and air temperature. Increase in snow is also related to the decrease in upward LWR due to the ground

Fig. 4 Anomalies of autumn (left column) SCE (unit: %) and (right column) SD (mm of water equivalent) obtained by regression against the standardized PC time series corresponding to **a, d** EOF1, **b, e** EOF2, and **c, f** EOF3 of the autumn Eurasian SAT anomalies. Stippling regions indicates anomalies significant at the 95% confidence level



temperature decrease. Furthermore, increase in snow may lead to increase in soil moisture when snow melts. This results in more upward surface latent heat flux (LHF) as the land–air humidity difference may increase. Note that change in SWR and LWR may also be impacted by total cloud cover (TCC). Hence, the TCC changes are also examined to understand generation of surface heat flux anomalies. Here, we examine anomalies of autumn surface net heat flux (NHF), SWR, LWR, SHF, LHF and TCC corresponding to the first three EOF modes. Surface heat flux anomalies are taken to be positive when their directions are downward, which contribute to surface warming.

Corresponding to the EOF1, positive NHF anomalies are seen around 60° – 70° and 50° – 140° E (Fig. 5a), which is mainly due to SHF increase (Fig. 5j). NHF anomalies are weak south of 60° N (Fig. 5a) due to cancellation among different components (Fig. 5d, g, j, m). Comparison of Fig. 4a, d with 5j indicates that SHF increase around 60° N cannot be explained by snow cover decrease there as snow cover decrease is expected to lead to SHF decrease (Ye et al. 2015; Chen et al. 2016b). SHF decrease around 50° N and 80° E may be partly due to snow decrease (Figs. 4a, d, 5j). SWR increase west of the Lake Baikal is attributed to

a combination of snow cover and TCC decreases (Fig. 4a, d, 5d, and 6a).

Corresponding to the EOF2, negative NHF anomalies extend from the East European Plain to north Europe (Fig. 5b). NHF anomalies are weak and insignificant east of the Lake Baikal where positive SAT anomalies are observed (Figs. 2c, 5b). SWR and LHF (LWR and SHF) have a negative (positive) contribution to the NHF increase over the north coast of Europe (Fig. 5b, e, h, k, n). NHF decrease north of the Caspian Sea and the Black Sea is mainly attributed to SWR and LHF (Fig. 5b, e, n). LWR and SHF increases have a negative contribution to the NHF decrease in those regions (Fig. 5b, h, k). SWR and LHF decreases as well as LWR and SHF increases north of the Caspian Sea and over the Black Sea may be related to the increase in SCE and SD (Figs. 4b, e, 5e, h, k, n). SWR and LWR changes north of the Caspian Sea and over the Black Sea cannot be explained by small TCC anomalies there (Fig. 6b). By contrast, SWR increase and LWR decrease over the north coast of Europe (Fig. 5e, h) cannot be explained by SCE increase (Fig. 4b, e), but may be attributed to TCC decrease (Fig. 6b). SHF decrease and LHF increase are not related to the snow changes over north coast of Europe (Figs. 4b, e, 5k, n).

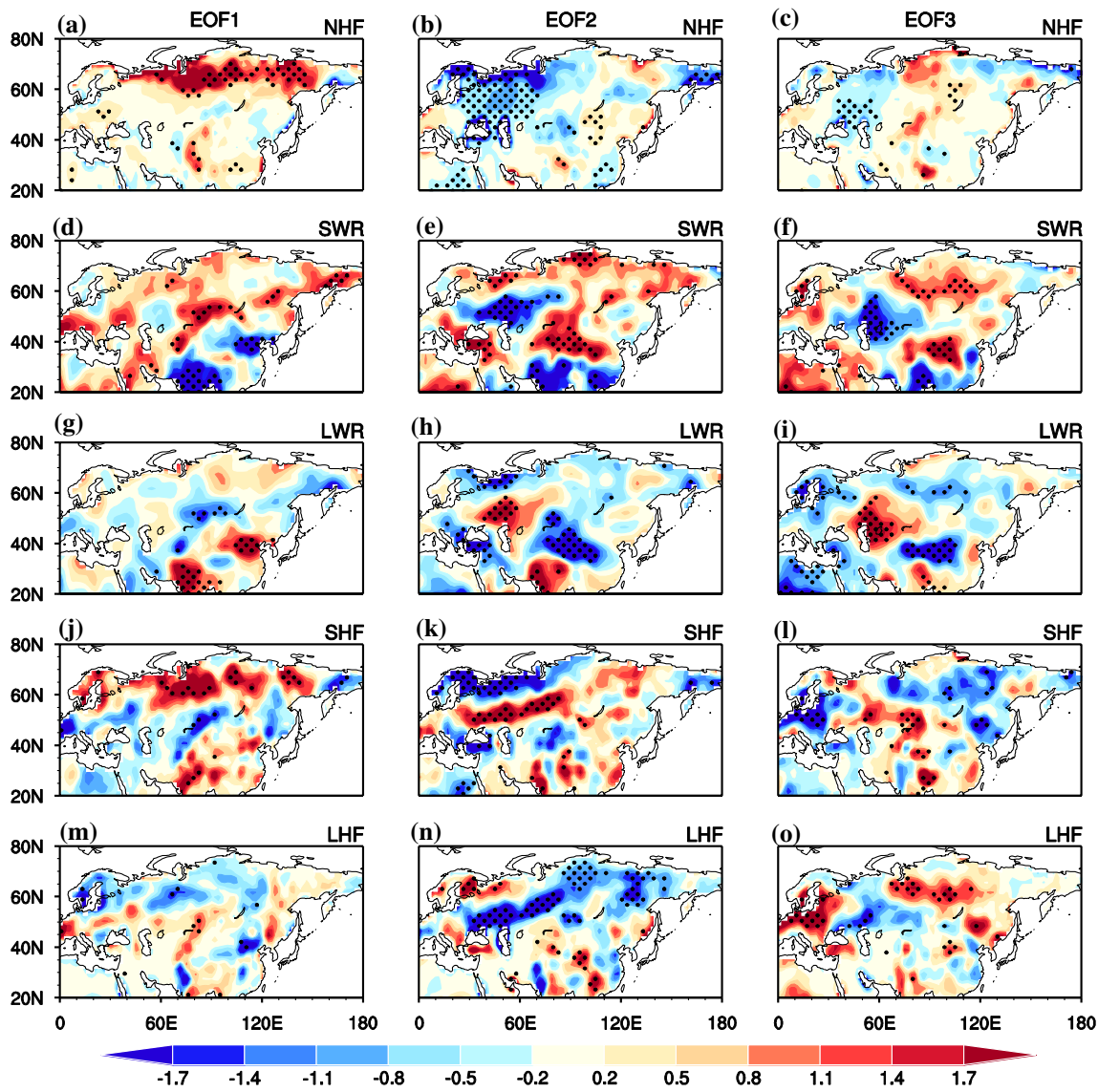


Fig. 5 Anomalies (unit: W m^{-2}) of autumn surface **a–c** net heat flux, **d–f** shortwave radiation, **g–i** longwave radiation, **j–l** sensible heat flux, and **m–o** latent heat flux obtained by regression against the standardized PC time series corresponding to (left column) EOF1,

(center column) EOF2, and (right column) EOF3 of autumn Eurasian SAT anomalies. Stippling regions indicate anomalies significant at the 95% confidence level

Corresponding to the EOF3, the spatial distribution of the NHF anomalies (Fig. 5c) displays notable difference from that of the SAT anomalies (Fig. 2e). This indicates that NHF change cannot explain the formation of the SAT anomalies. SWR decrease and LWR increase northeast of the Caspian Sea cannot be explained by weak SCE and SD anomalies. SWR and LWR changes around 70°E seem to be related well to TCC change (Figs. 5f, i, 6c). In particular, TCC increase (decrease) generally corresponds to LWR increase (decrease) and SWR decrease (increase). The SHF increase around the 50°N and 80°E may be partly related to the increase in SCE and SD (Figs. 4c, f, 5l).

Above analysis of surface heat flux changes suggests that snow cover changes over many regions cannot explain the formation of SAT anomalies related to the first three EOF modes. This implies that the atmospheric anomalies may play important roles in the interannual variability of SAT anomalies over Eurasia. Roles of the atmospheric anomalies in the SAT changes are examined in the following section.

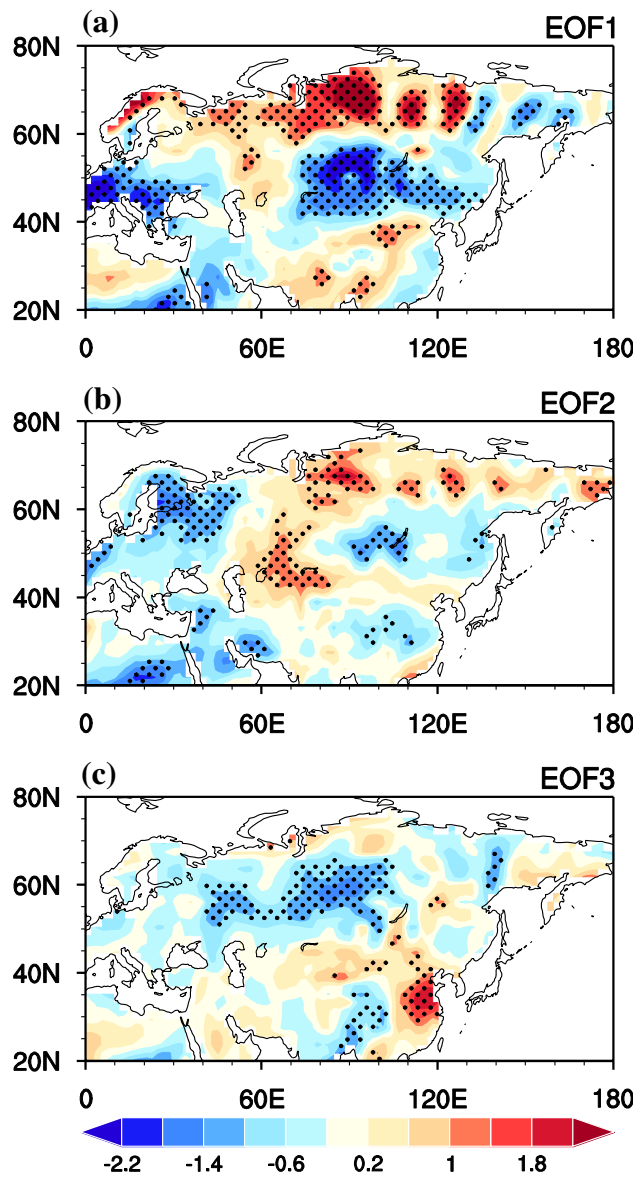


Fig. 6 Anomalies of autumn TCC (unit: %) obtained by regression against the standardized PC time series corresponding to **a** EOF1, **b** EOF2, and **c** EOF3 of autumn Eurasian SAT anomalies. Stippling regions indicate anomalies significant at the 95% confidence level

5 Contributions of atmospheric circulation anomalies

The spatial distributions of the SAT anomalies for the first three EOF modes match well with those of surface wind anomalies (Figs. 2a, c, e and 7a–c). Corresponding to the EOF1, strong cyclonic wind anomalies are observed over the north coast of Eurasia and Barents–Kara seas, and anticyclonic anomalies are observed over west Europe and the Lake Baikal (Fig. 7a). Accordingly, southwesterly wind anomalies appear over the mid-high latitudes of Eurasia, and northerly wind anomalies occur over the Mediterranean.

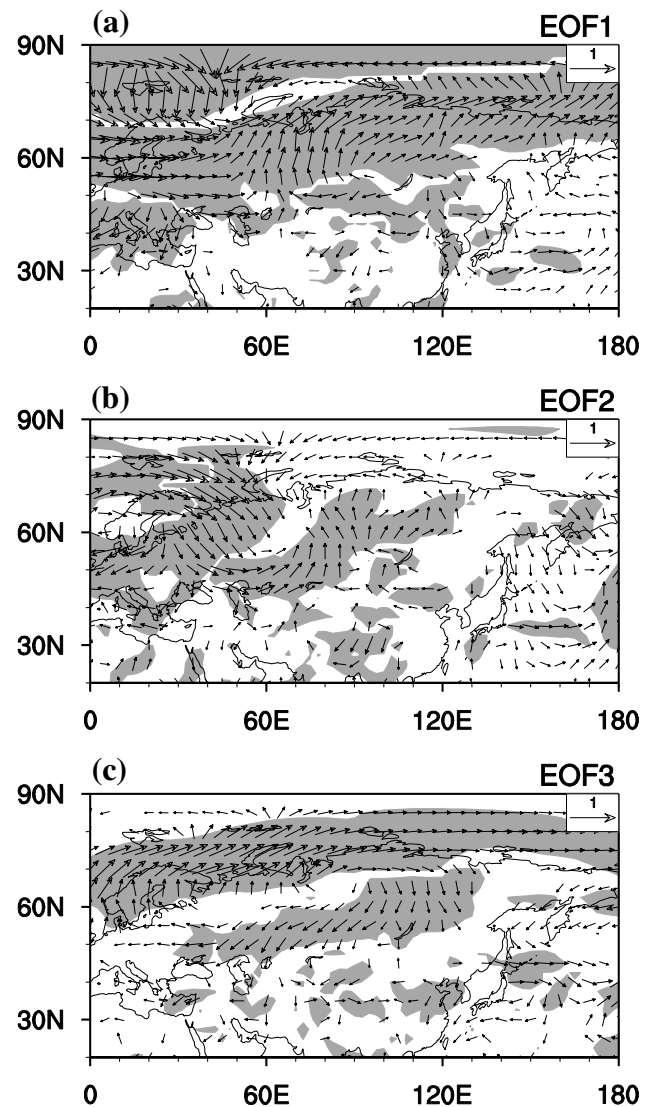


Fig. 7 Anomalies (unit: m s^{-1}) of autumn surface (10 m) winds obtained by regression against the standardized PC time series of **a** EOF1, **b** EOF2, and **c** EOF3 of autumn Eurasian SAT anomalies. Shading regions indicates either component of the wind anomalies that are significantly different from zero at the 95% confidence level. Wind anomalies in both directions less than 0.08 m s^{-1} are masked

The southwesterly wind anomalies contribute to the positive SAT anomalies over the mid-high latitudes of Eurasia via bringing warmer air from lower latitudes (Figs. 2a, 7a). The negative SAT anomalies around the Balkan Peninsula are due to the northerly wind anomalies there, which bring colder air from higher latitudes (Figs. 2a, 7a). The anticyclonic anomaly over the Lake Baikal leads to less TCC and results in more SWR reaching the surface, contributing to positive SAT anomalies there (Figs. 2a, 5a, 7a).

Corresponding to the EOF2, anticyclonic wind anomalies are observed over North Europe and cyclonic wind anomalies are seen over West Siberia (Fig. 7b). An anomalous

anticyclone, but with smaller amplitude, can also be observed around the Lake Baikal. In correspondence, northerly wind anomalies are seen over the East European Plain and southerly wind anomalies extend from north of the Caspian Sea to north of the Lake Baikal. The northerly wind anomalies over the East European Plain bring colder air from higher latitudes, leading to negative SAT anomalies there (Figs. 2c, 7b). By contrast, positive SAT anomalies north of the Lake Baikal are attributable to southerly wind anomalies.

Corresponding to the EOF3, an anomalous anticyclone is present over north part of the Eurasia, inducing southwesterly wind anomalies over the north coast of the Eurasia and northeasterly wind anomalies over central Siberia (Fig. 7c). The southwesterly wind anomalies contribute to positive SAT anomalies over the north coast of the Eurasia (Figs. 2e,

7c). Negative SAT anomalies over the central Siberia are related to northeasterly wind anomalies there (Figs. 2e, 7c).

Above results imply that atmospheric anomalies are crucial for interannual variability of autumn SAT over the mid-high latitudes of Eurasia. In general, southerly (northerly) wind anomalies bring warmer (colder) air from lower (higher) latitudes and result in positive (negative) SAT anomalies. In the following, we further discuss the plausible factors for the formation of the atmospheric anomalies related to the first three EOF modes of the Eurasian autumn SAT interannual variations. The atmospheric anomalies over Eurasia may be associated with large-scale atmospheric variability beyond Eurasia.

Atmospheric anomalies related to the first three EOF modes all display a barotropic vertical structure (Fig. 8). For the EOF1 mode, a cyclonic anomaly appears over Eurasian

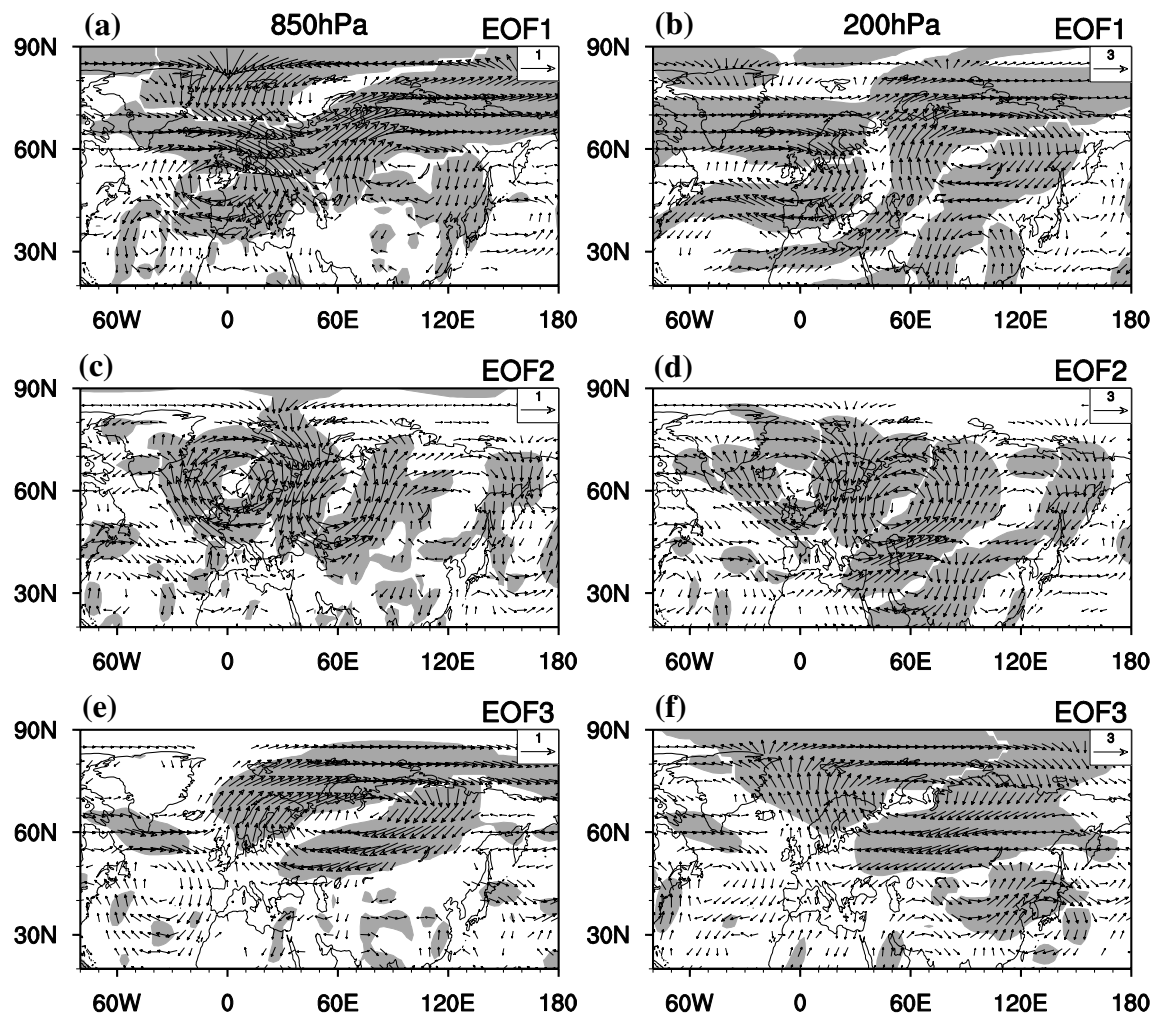


Fig. 8 Anomalies (unit: m s^{-1}) of (left column) 850 hPa and (right column) 200 hPa wind anomalies obtained by regression against the standardized PC time series corresponding to **a, b** EOF1, **c, d** EOF2, and **e, f** EOF3 of autumn Eurasian SAT anomalies. Shading regions

indicates either component of the wind anomalies that are significantly different from zero at the 95% confidence level. Wind anomalies at 850 hPa (200 hPa) in both directions less than 0.1 (0.2) m s^{-1} are masked

Arctic region and two anticyclonic anomalies occur over west Europe and around the Lake Baikal regions, respectively (Fig. 8a, b). Correspondingly, southwesterly wind anomalies are seen over the mid-high latitudes of Eurasia and northerly wind anomalies are present over east coast of East Asia and around the Mediterranean Sea. For the EOF2 mode, a clear atmospheric wave train is observed to extend from the mid-latitudes of the North Atlantic to the high-latitudes of the North Atlantic and north Europe, and then eastward to East Asia (Fig. 8c, d). For the EOF3 mode, a pronounced anticyclonic anomaly dominates over the high latitudes of Eurasia and around the Barents–Kara seas (Fig. 8e, f).

For the EOF1, negative 500 hPa geopotential height anomalies appear over the Arctic region (Fig. 9a). This

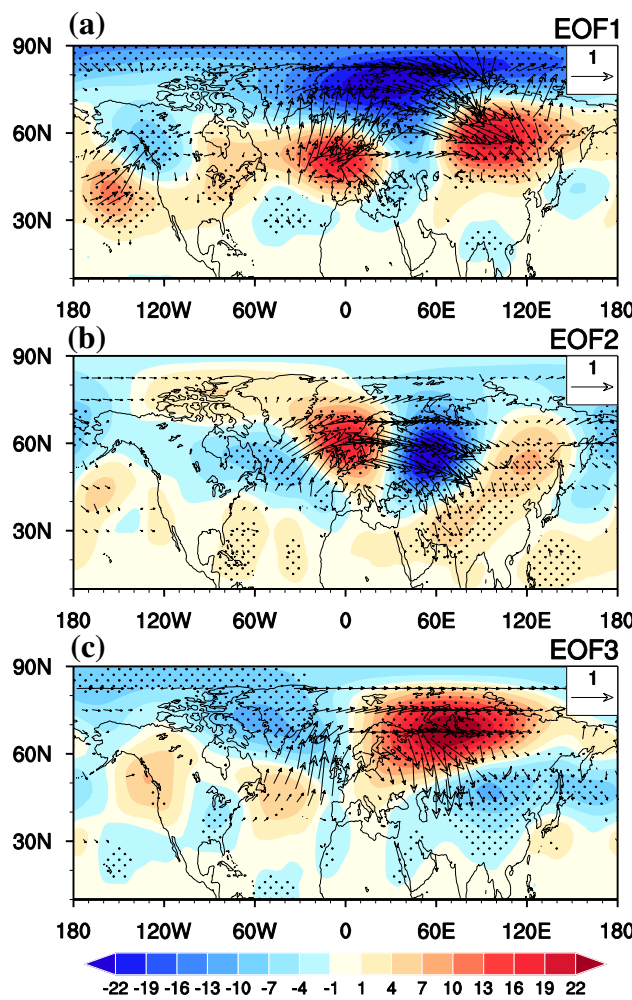


Fig. 9 Anomalies of autumn 500 hPa geopotential height (shadings; unit: gpm) and wave activity fluxes (vectors; unit: $\text{m}^2 \text{s}^{-2}$) obtained by regression against the standardized PC time series of **a** EOF1, **b** EOF2, and **c** EOF3 of autumn Eurasian SAT anomalies. Stippling regions indicates geopotential height anomalies that are significantly different from zero at the 95% confidence level. Wave activity flux anomalies in both directions less than $0.05 \text{ m}^2 \text{s}^{-2}$ are masked

structure is reminiscent of the AO (Thompson and Wallace 2000). The correlation coefficient between the autumn AO index and the PC time series of the EOF1 reaches 0.61 during 1948–2014, significant at the 99.9% confidence level. This suggests that the AO related atmospheric circulation anomalies play an important role in modulating the SAT anomalies related to the first EOF mode. Correlation of the EOF1 with the NAO is much weaker than that with the AO (Table 1). Furthermore, an atmospheric wave train is observed over west Europe through the Scandinavian Peninsula and then southeastward to the region around the Lake Baikal (Fig. 9a). This atmospheric wave train resembles closely the SCAND teleconnection pattern (Barnston and Livezey 1987; Chen et al. 2018a). The correlation coefficient between the SCAND pattern index and the PC1 time series reaches -0.63 , slightly larger than that related to the autumn AO ($r=0.61$) (Table 1). This indicates that the SCAND teleconnection pattern is another important factor for the interannual variation of the autumn SAT anomalies over the mid-high latitudes of Eurasia. Correlations of the other atmospheric teleconnection patterns (such as EA, EAWR, PNA, WP and CGT) with the first EOF mode are weak (Table 1).

To further confirm roles of the AO and SCAND pattern in the interannual variation of Eurasian SAT, we present autumn SAT and 850 hPa wind anomalies related to autumn AO and SCAND pattern indices in Fig. 10. Positive SAT anomalies are seen over most regions of Eurasia north of 40°N during positive phases of the autumn AO and negative phase of the SCAND pattern (Fig. 10a, b). This is attributed to southwesterly wind anomalies related to the autumn AO and SCAND pattern (Fig. 10c, d). In comparison, the positive SAT anomalies related to the AO shift relatively northward compared to those related to the SCAND pattern. Differences in the SAT anomalies over Eurasia (Fig. 10a, b) are associated with the structure of atmospheric circulation anomalies related to the AO and SCAND pattern (Fig. 10c,

Table 1 Correlation coefficients of PC1, PC2, and PC3 time series of autumn Eurasian SAT interannual variations with different teleconnection indices at simultaneous autumn

	PC1	PC2	PC3
AO	0.61**	0.017	0.09
NAO	0.30*	0.034	0.24
EA	-0.13	-0.03	0.02
EAWR	0.07	0.72**	-0.19
PNA	-0.03	0.11	-0.02
SCAND	-0.63*	0.16	0.17
WP	-0.19	0.03	-0.16
CGT	0.19	0.40*	-0.2

“*” and “**” indicate correlation coefficient significant at the 95% and 99% confidence level, respectively

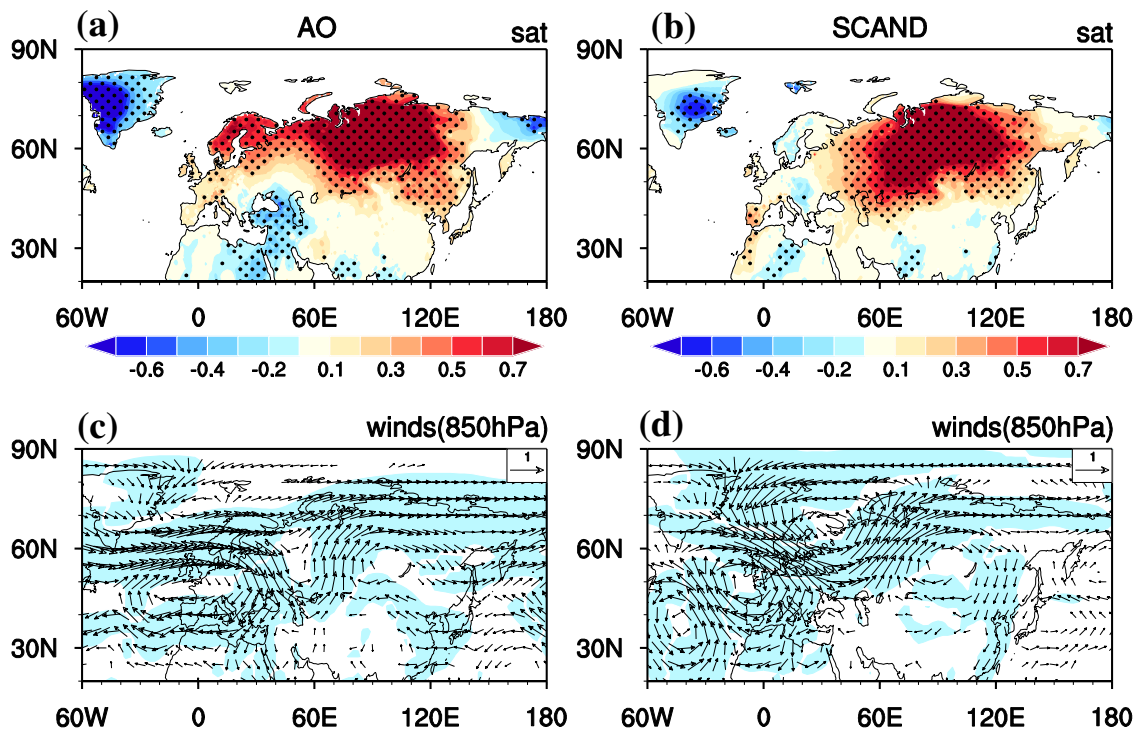


Fig. 10 Anomalies of autumn **a, b** SAT (unit: $^{\circ}\text{C}$), and **c, d** winds (unit: m s^{-1}) at 850 hPa obtained by regression against the standardized autumn (left column) AO index and (right column) minus one SCAND teleconnection index, respectively. Stippling regions in **a, b** indicate SAT anomalies that are significantly different from zero

at the 95% confidence level. Shading regions in **c, b** indicates either component of the wind anomalies that are significantly different from zero at the 95% confidence level. Wind anomalies in both directions less than 0.1 m s^{-1} are masked

d). Overall, above evidences verify that autumn AO and SCAND related atmospheric anomalies are two important factors for the SAT anomalies over mid-high latitudes of Eurasia related to the EOF1.

For the EOF2, a clear atmospheric wave train extends from the North Atlantic to East Asia (Fig. 9b). This atmospheric wave train bears a close resemblance to the EAWR pattern (Barnston and Livezey 1987). The correlation coefficient between the PC2 time series and the EAWR index is as high as 0.72 during 1948–2014, significant at the 99.9% confidence level (Table 1). This implies that EAWR-related atmospheric anomalies play a key role in modulating the SAT anomalies related to the EOF2. In addition, the CGT pattern has a correlation coefficient of 0.4 with the PC2 time series (Table 1), significant at the 95% confidence level. This indicates that the CGT pattern may also play a role in modulating the autumn SAT anomalies over the mid-high latitudes of Eurasia related to the EOF2. Figure 11 shows autumn SAT and 850 hPa wind anomalies obtained by regression against the standardized autumn EAWR and CGT indices, respectively. The EAWR and CGT pattern related autumn SAT anomalies both display an east–west dipole pattern over the mid-high latitudes of Eurasia (Fig. 11a, b), similar to the structure of the SAT anomalies related to the EOF2 (Fig. 2c).

The positive SAT anomalies over East Siberia related to the EAWR and CGT pattern are attributed to southerly wind anomalies there (Fig. 11a, d). By contrast, negative SAT anomalies over the west Siberia are resulted from northerly wind anomalies related to the EAWR and CGT pattern. Above results confirm that the EAWR and the CGT patterns play important roles in the formation of the SAT anomalies related to the EOF2.

For the EOF3, correlations of the atmospheric teleconnection patterns with the PC3 time series are weak and insignificant (Table 1). An atmospheric wave train originates from Eurasian Arctic and extends southeastward to East Asia (Fig. 9c). This result implies that the formation of the atmospheric anomalies over Eurasia related to the EOF3 may be partly attributed to the Arctic sea ice change. Actually, the spatial structure of the atmospheric anomalies over Eurasia related to the EOF3 bear a close resemblance to that related to decrease in the Arctic sea ice around the Barents–Kara Sea as identified in Wu et al. (2016). Wu et al. (2016) demonstrated that decrease in the Arctic sea ice concentration around the Barents–Kara Sea can induce an atmospheric wave train from Eurasian Arctic to East Asia, with a significant anticyclone around the high latitudes of the Eurasia (see their Fig. 3). To check the possible role

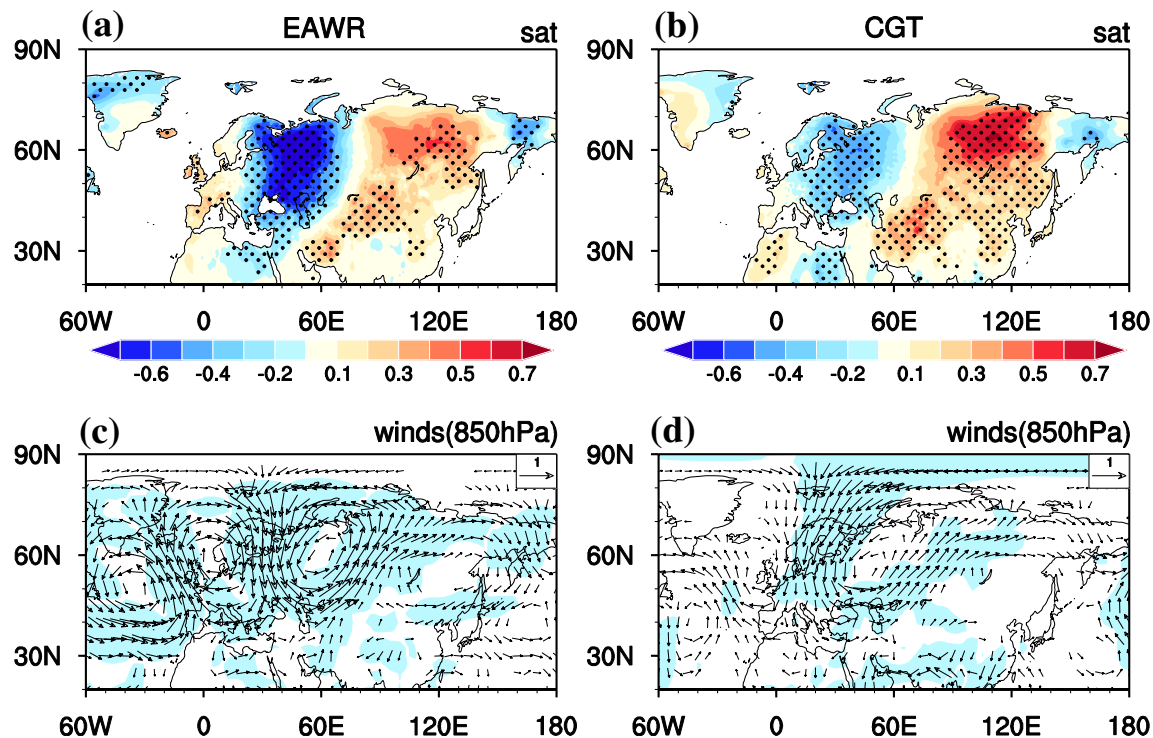


Fig. 11 Anomalies of autumn **a, b** SAT ($^{\circ}$ C), and **c, d** winds ($m s^{-1}$) at 850 hPa obtained by regression against the standardized autumn (left column) EAWR and (right column) CGT teleconnection indices, respectively. Stippling regions in **a, b** indicate SAT anomalies that are

significantly different from zero at the 95% confidence level. Shading regions in **c, b** indicates either component of the wind anomalies that are significantly different from zero at the 95% confidence level. Wind anomalies in both directions less than $0.1 m s^{-1}$ are masked

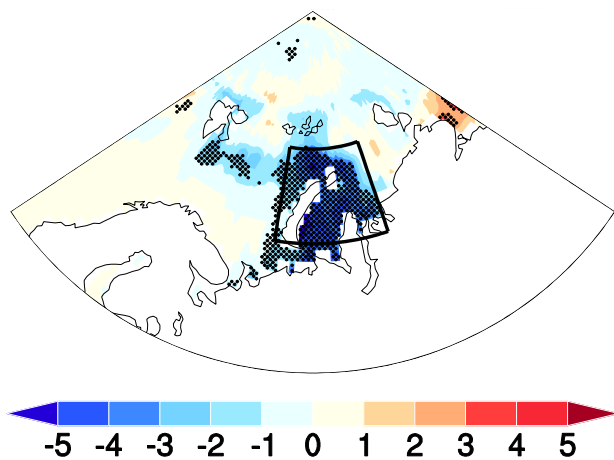


Fig. 12 Anomalies of autumn Arctic sea ice cover (SIC; unit: %) obtained by regression against the PC time series of EOF3 of autumn Eurasian SAT anomalies. Stippling regions indicate SIC anomalies significant at the 95% confidence level

of the Arctic sea ice change in the formation of the atmospheric anomalies related to the EOF3, we show Arctic sea ice anomalies related to the PC3 time series in Fig. 12. Significant decrease in the Arctic sea ice is seen around the Barents–Kara Seas related to the EOF3. Based on the results in

Fig. 12, an Arctic sea ice index (ASI) is defined using area-averaged sea ice concentration anomalies over 70° – 79° N and 30° – 80° E (Fig. 13). The original autumn ASI shows a significant decreasing trend during 1948–2014 (Fig. 13), consistent with previous studies (Liu et al. 2012; Wu et al. 2016). The correlation coefficient between interannual variation of the autumn ASI and the PC3 time series reaches -0.46 during 1948–2014, significant at the 99% confidence level. It is noted that a significant correlation ($r = -0.51$) is still observed for the period 1979–2014 between the autumn ASI and the PC3.

We further examine anomalies of autumn SAT and 850 hPa winds anomalies related to the standardized minus one ASI index. An anticyclonic anomaly occurs over the high latitudes of Eurasia related to decrease in the ASI (Fig. 14b), consistent with Wu et al. (2016). The SAT anomalies related to the ASI index display a south–north dipole pattern (Fig. 14a), similar to the SAT anomalies related to the EOF3. Hence, change in the ASI around the Barents–Kara Seas may partly contribute to the SAT anomalies related to the EOF3. Nevertheless, other factors may also play an important role in the SAT anomalies related to the EOF3, which remain to be explored.

SST anomalies in the North Atlantic Ocean may modulate Eurasian SAT anomalies during boreal spring and summer

Fig. 13 Normalized time series of the original autumn Arctic sea ice index (ASI) (blue line) and its interannual component (red line) during 1948–2014. The autumn ASI is defined as area-mean SIC anomalies over $70^{\circ}\text{--}79^{\circ}\text{N}$ and $30^{\circ}\text{--}80^{\circ}\text{E}$

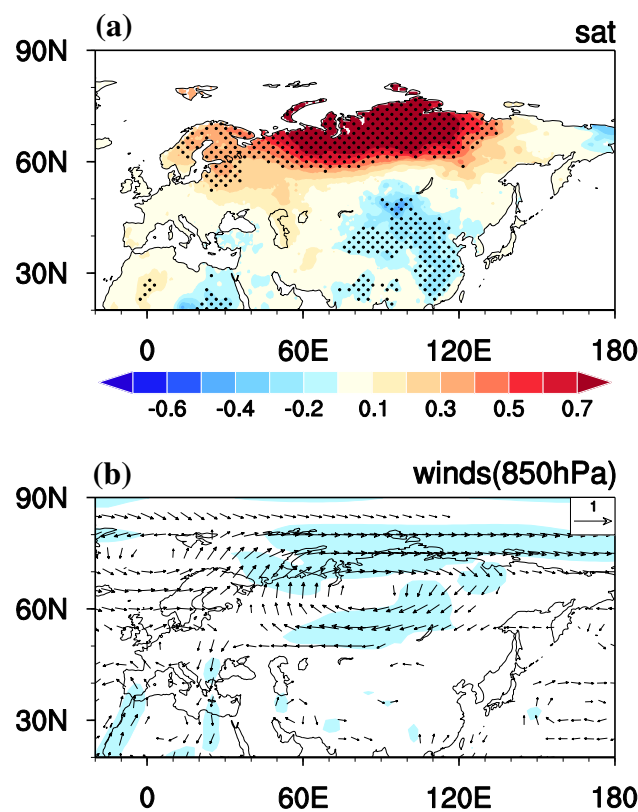
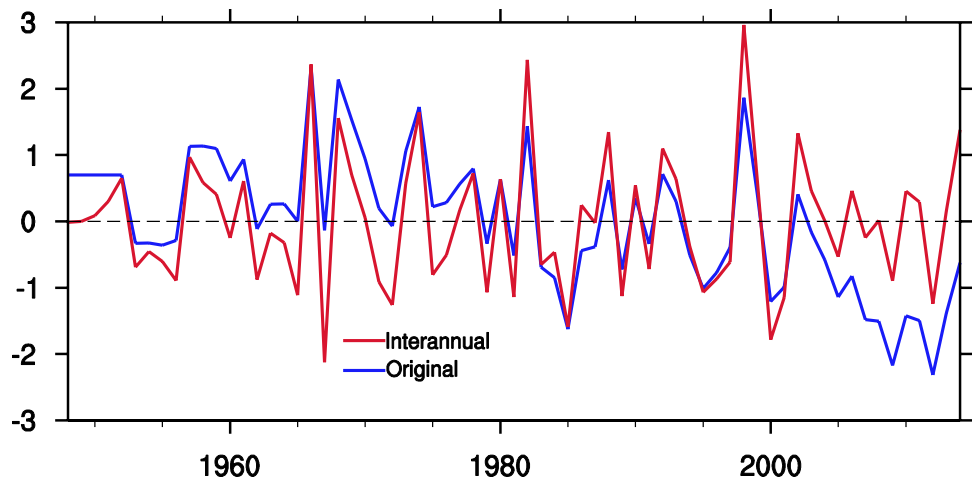


Fig. 14 Anomalies of autumn **a** SAT (unit: $^{\circ}\text{C}$), and **b** winds (unit: m s^{-1}) at 850 hPa obtained by regression against the standardized interannual variation of the autumn ASI. Stippling regions in **a** indicate SAT anomalies that are significantly different from zero at the 95% confidence level. Shading regions in **b** indicates either component of the wind anomalies that are significantly different from zero at the 95% confidence level. Wind anomalies in both directions less than 0.1 m s^{-1} are masked. Definition of the Autumn SIC index is provided in the text

via triggering an atmospheric wave train (Wu et al. 2009, 2011; Chen et al. 2016b, 2018b, c). Hence, a question is: Do SST anomalies have a role in the generation of the

atmospheric circulation anomalies related to the first three EOF modes of the autumn SAT anomalies over the mid-high latitudes of Eurasia? To address this issue, we display SST anomalies obtained by regression upon the PC time series of the first three EOF modes in Fig. 15. The obtained SST anomalies are generally weak in the North Atlantic, Indian Ocean and North Pacific except for small patch of significant anomalies south of Japan (Fig. 15). This indicates that atmospheric circulation anomalies related to the first three EOF modes of autumn Eurasian SAT may not be related to the SST anomalies.

6 Empirical model of autumn Eurasian SAT anomalies

Above results indicate that the AO and SCAND teleconnection patterns both play important roles in autumn Eurasian SAT anomalies related to the EOF1. In addition, autumn Eurasian SAT anomalies related to EOF2 are impacted by the EAWR and CGT patterns. In the following, we establish empirical models to hindcast the PC1 (PC2) time series of autumn Eurasian SAT variations based on both the AO and SCAND indices (EAWR and CGT indices), respectively. The empirical models are presented as follows:

$$\text{PC1}(t) = a_1 \times \text{AO_res}(t) + b_1 \times \text{SCAND_res}(t), \quad (1)$$

$$\text{PC2}(t) = a_2 \times \text{EAWR_res}(t) + b_2 \times \text{CGT_res}(t), \quad (2)$$

where t denotes time in years. $\text{PC1}(t)$ and $\text{PC2}(t)$ represent PC1 and PC2 time series of autumn Eurasian SAT, respectively. AO_res (SCAND_res) denotes the part of autumn SCAND (AO) index that is linearly unrelated to the autumn SCAND (AO) index. In addition, EAWR_res (CGT_res) indicates the part of autumn EAWR (CGT) index that is linearly unrelated to the autumn CGT (EAWR) index. The hindcast skills of these empirical models are cross validated

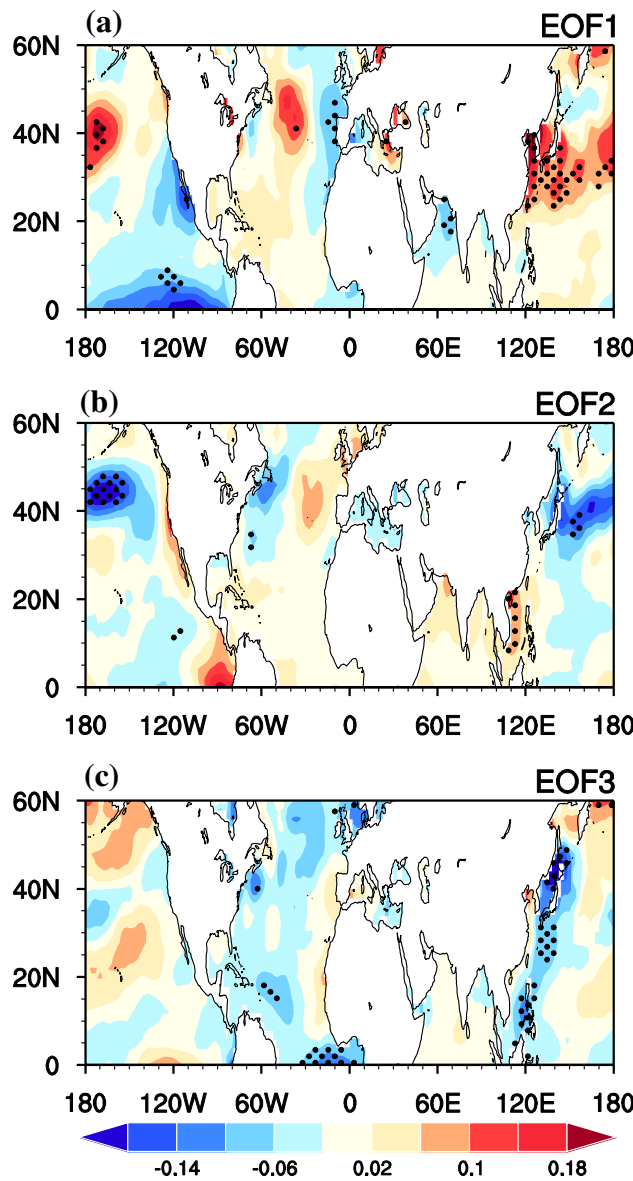


Fig. 15 Anomalies of autumn SST (unit: $^{\circ}\text{C}$) obtained by regression against the standardized PC time series of **a** EOF1, **b** EOF2, and **c** EOF3 of Autumn Eurasian SAT anomalies, respectively. Stippling regions indicate SST anomalies significant at the 95% confidence level

via a leave-one-out scheme (i.e., excluding 1 year from the period 1950–2014, determining the regression coefficient via remaining indices and then hindcasting the value for the excluded year) (Ham et al. 2013; Chen et al. 2018b). The results are shown in Fig. 16.

When both the AO and SCAND indices are used to hindcast the PC1 time series, the cross validated correlation coefficient is 0.72, which is much higher than that only using the autumn AO ($R=0.35$) or SCAND ($R=0.37$) to predict the PC1 time series. In particular, extreme values of the PC1 time series in most of the years are better hindcasted by the empirical

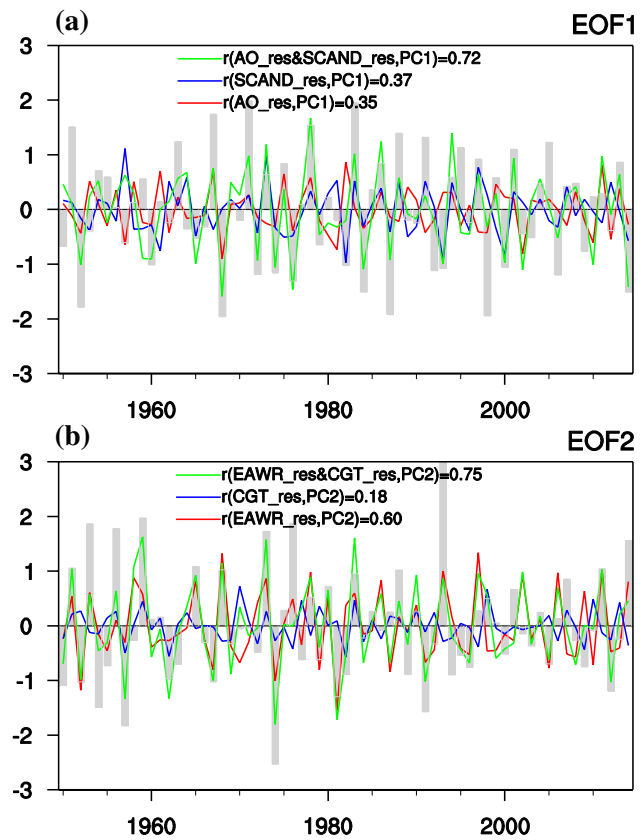


Fig. 16 **a** Standardized PC1 time series of autumn Eurasian SAT during 1950–2014 (black bars), and the cross-validated hindcasts of the PC1 time series by empirical models using the autumn AO_{res} index alone (red line), using the autumn SCAND_{res} index alone (blue line), and using both the Autumn AO_{res} and SCAND_{res} indices (green line). **b** Standardized PC2 time series of autumn Eurasian SAT (black bars), and the cross-validated hindcasts of the PC2 time series by empirical models using the autumn EAWR_{res} index alone (red line), using the autumn CGT_{res} index alone (blue line), and using both the autumn EAWR_{res} and CGT_{res} indices (green line)

model when both the AO and SCAND are taken into account (Fig. 16a). The cross validated correlation coefficient is 0.72 when both the EAWR and CGT indices are employed to hindcast the PC2 time series. This is also higher than that only using EAWR ($R=0.60$) or CGT ($R=0.18$) to predict the PC2 time series. In addition, amplitudes of the PC2 time series in many years are better reproduced by the empirical model when using both the EAWR and CGT indices (Fig. 16b). Therefore, above results show that the hindcast skill of autumn Eurasian SAT anomalies related to the EOF1 (EOF2) may be improved when both the AO and SCAND (EAWR and CGT) indices are considered.

7 Summary

This study analyzed boreal autumn SAT variations over the mid-high latitudes of Eurasia on the interannual timescale during 1948–2014 and the plausible factors. An EOF technique was first employed to obtain the dominant modes of the autumn Eurasian SAT interannual variations. The first EOF mode is characterized by same-sign SAT anomalies over the mid-high latitudes of Eurasia. The second EOF mode is featured by an east–west dipole anomaly pattern, with one center of SAT anomalies over the East Europe Plain and the other center of opposite sign located north of the Lake Baikal. The third EOF mode displays a south–north dipole pattern, with large SAT anomalies over the north coast of the Eurasia and anomalies with opposite sign over the central Siberia.

Then, we analyzed the possible contribution of the snow cover change to the SAT anomalies via analysis of the surface heat fluxes. For the first EOF mode, snow changes can partly contribute to SAT anomalies around the central Siberia via modulating surface shortwave radiation. Formation of the SAT anomalies in other regions is not related to the snow changes. For the second EOF mode, negative SAT anomalies over the East Europe Plain may be partly attributed to the pronounced increase in snow cover. Increase in snow cover leads to increase in surface albedo and results in decrease in downward SWR, which further contributes to negative SAT anomalies. Snow anomalies related to the EOF2 are weak around the Lake Baikal. Hence, the positive SAT anomalies related to the EOF2 around the Lake Baikal are not due to the snow changes. For the EOF3, surface heat flux anomalies are weak. This implies that snow changes may play little role in the SAT anomalies related to the EOF3.

Further analyses show that atmospheric circulation anomalies play an important role in the SAT anomalies related to the dominant modes of the autumn Eurasian SAT interannual variations. For the EOF1, positive SAT anomalies over most regions of the Eurasia are related to southwesterly wind anomalies, which bring warmer air from lower latitudes. For the EOF2, negative SAT anomalies over the East Europe Plain are attributed to northerly wind anomalies. The northerly wind anomalies carry colder air from higher latitudes and lead to negative SAT anomalies. By contrast, positive SAT anomalies around the Lake Baikal are related to southerly wind anomalies that transport warmer air from lower latitudes. For the EOF3, positive SAT anomalies over the north coast of Eurasia are associated with southwesterly wind anomalies, and negative SAT anomalies over the central Siberia are related to northeasterly winds anomalies there.

We further investigate the factors for the formations of the atmospheric circulation anomalies related to the

first three EOF modes. For the EOF1 mode, the atmospheric circulation over Eurasia has a close relationship with the AO and SCAND teleconnection patterns. This implies that the AO and SCAND patterns collectively contribute to the continent-scale same-sign SAT anomalies over the mid-high latitudes of Eurasia. For the EOF2 mode, atmospheric anomalies display a clear wave train over the North Atlantic through Eurasia, with anticyclonic anomalies over west Europe and East Asia and cyclonic anomalies over the mid-latitudes of the North Atlantic and over the west Siberia. The EAWR and CGT patterns have an important contribution to the atmospheric circulation anomalies related to the EOF2 mode. This indicates that the EAWR and CGT patterns play an important role in the formation of the east–west dipole SAT anomalies over the mid-high latitudes of Eurasia during boreal autumn. For the EOF3 mode, anticyclonic anomaly over the high latitudes of the Eurasia, which may be partly attributed to the Arctic sea changes, plays a key role in the generation of the south–north dipole SAT anomalies. In addition, atmospheric circulation anomalies related to the first three EOF modes do not have a clear relationship with the SST anomalies.

Furthermore, we have developed empirical models to hindcast PC1 (PC2) time series of the Eurasian autumn SAT variations via employing a combination of the autumn AO and SCAND (EAWR and CGT) indices. The results show that the cross validated correlation coefficients of the empirical model are much higher than those employing only the autumn AO or SCAND index to forecast the EOF1 mode of the Eurasian autumn SAT variation. The cross validated correlation coefficients of the empirical model are also higher than those employing only the autumn EAWR or CGT index to forecast the EOF2 mode of the Eurasian autumn SAT variation. This indicates that the AO and SCAND patterns are both important for the prediction of continent-wide same-sign SAT anomalies over the mid-high latitudes of Eurasia during boreal autumn. Furthermore, the EAWR and CGT are both crucial for the prediction of the autumn east–west dipole SAT anomalies.

Acknowledgements We thank two anonymous reviewers for their constructive suggestions, which helped to improve the paper. This study is supported by the National Key Research and Development Program of China (Grant no. 2018YFA0605604), the National Natural Science Foundation of China Grants (41530425, 41775080, 41721004, and 41605031), and the Young Elite Scientists Sponsorship Program by the China Association for Science and Technology (2016QNRC001).

References

- Barnett T, Dümenil L, Schlese U, Roeckner E, Latif M (1989) The effect of Eurasian snow cover on regional and global climate

- variations. *J Atmos Sci* 46:661–686. [https://doi.org/10.1175/1520-0469\(1989\)046,0661:TEOESC.2.0.CO;2](https://doi.org/10.1175/1520-0469(1989)046,0661:TEOESC.2.0.CO;2)
- Barnston AG, Livezey RE (1987) Classification, seasonality and persistence of low-frequency atmospheric circulation patterns. *Mon Wea Rev* 115:1083–1126
- Barriopedro D, Fischer EM, Luterbacher J, Trigo RM, Garcíá-Herrera R (2011) The hot summer of 2010: redrawing the temperature record map of Europe. *Science* 332:220–224. <https://doi.org/10.1126/science.1201224>
- Brodzik M, Armstrong R (2013) Northern Hemisphere EASE-Grid 2.0 weekly snow cover and sea ice extent, version 4. National Snow and Ice Data Center, Boulder, CO, digital media. [Available online at <http://nsidc.org/data/nsidc-0046>.]
- Caloiero T (2017) Trend of monthly temperature and daily extreme temperature during 1951–2012 in New Zealand. *Theor Appl Climatol* 129:111–127
- Chen S, Song L (2018) The leading interannual variability modes of winter surface air temperature over Southeast Asia. *Clim Dyn*. <https://doi.org/10.1007/s00382-018-4406-x>
- Chen S, Wu R (2018) Impacts of early autumn arctic sea ice concentration on subsequent spring Eurasian surface air temperature variations. *Clim Dyn* 51:2523–2542. <https://doi.org/10.1007/s00382-017-4026-x>
- Chen Z, Wu R, Chen W (2014) Impacts of autumn arctic sea ice concentration changes on the East Asian winter monsoon variability. *J Clim* 27:5433–5450. <https://doi.org/10.1175/JCLI-D-13-00731.1>
- Chen W, Hong X, Lu R, Jin A, Jin S, Nam J, Shin J, Goo T, Kim B (2016a) Variation in summer surface air temperature over northeast Asia and its associated circulation anomalies. *Adv Atmos Sci* 33:1–9. <https://doi.org/10.1007/s00376-015-5056-0>
- Chen S, Wu R, Liu Y (2016b) Dominant modes of interannual variability in Eurasian surface air temperature during boreal spring. *J Clim* 29:1109–1125. <https://doi.org/10.1175/JCLI-D-15-0524.1>
- Chen S, Wu R, Song L, Chen W (2018a) Combined influences of the arctic oscillation and the Scandinavia pattern on spring surface air temperature variations over Eurasia. *J Geophys Res* 123:9410–9429. <https://doi.org/10.1029/2018JD028685>
- Chen S, Wu R, Chen W (2018b) Modulation of spring northern tropical Atlantic sea surface temperature on the El Niño–Southern Oscillation–East Asian summer monsoon connection. *Int J Climatol* 38:5020–5029. <https://doi.org/10.1002/joc.5710>
- Chen S, Wu R, Chen W, Yao S (2018c) Enhanced linkage between Eurasian winter and spring dominant modes of atmospheric interannual variability since the early-1990s. *J Clim* 31:3575–3595
- Cheung HN, Zhou W (2015) Implications of ural blocking for East Asian winter climate in the CMIP5 models. Part I: biases in the historical scenario. *J Clim* 28:2203–2216. <https://doi.org/10.1175/JCLI-D-14-00308.1>
- Cheung HN, Zhou W, Mok HY, Wu MC (2012) Relationship between ural-Siberian blocking and East Asian winter monsoon in relation to Arctic oscillation and El Niño/Southern oscillation. *J Clim* 25:4242–4257
- Cohen J, Furtado J, Barlow M, Alexeev V, Cherry J (2012) Arctic warming, increasing fall snow cover and widespread boreal winter cooling. *Environ Res Lett* 7:014007
- Cohen J, Screen JA, Furtado JC, Barlow M, Whittleston D, Coumou D, Francis J, Dethloff K, Entekhabi D, Overland J, Jones J (2014) Recent Arctic amplification and extreme mid-latitude weather. *Nat Geosci* 7:627–637
- D'Arrigo R, Wilson R, Li J (2006) Increased Eurasian-tropical temperature amplitude difference in recent centuries: implications for the Asian monsoon. *Geophys Res Lett* 33:L22706. <https://doi.org/10.1029/2006GL027507>
- Dee DP et al (2011) The ERA-Interim reanalysis: configuration and performance of the data assimilation system. *Quart J Roy Meteor Soc* 137:553–597. <https://doi.org/10.1002/qj.828>
- Ding Q, Wang B (2005) Circumglobal teleconnection in the Northern hemisphere summer. *J Clim* 18:3483–3505
- Duchon C (1979) Lanczos filtering in one and two dimensions. *J Appl Meteorol* 18:1016–1022
- Feudale L, Shukla J (2010) Influence of sea surface temperature on the European heat wave of 2003 summer. Part I: an observational study. *Clim Dyn* 36:1691–1703. <https://doi.org/10.1007/s00382-010-0788-0>
- Gong D, Wang S, Zhu J (2001) East Asian winter monsoon and Arctic oscillation. *Geophys Res Lett* 28:2073–2076
- Ham YG, Kug JS, Park JY, Jin FF (2013) Sea surface temperature in the north tropical Atlantic as a trigger for El Niño/Southern Oscillation events. *Nat Geosci* 6:112–116
- Henderson-Sellers A (1996) Soil moisture: a critical focus for global change studies. *Global Planet Change* 13:3–9
- Hurrell JW, van Loon H (1997) Decadal variations in climate associated with the North Atlantic Oscillation. In: Diaz HF, Beniston M, Bradley R (eds) *Climatic change at high elevation sites*. Springer, Berlin, pp 69–94
- IPCC (2013) Summary for policymakers. Fifth Assessment report of the Intergovernmental panel on climate change. Cambridge University Press, Cambridge
- Jhun JG, Lee EJ (2004) A new East Asian winter monsoon index and associated characteristics of the winter monsoon. *J Clim* 17:711–726
- Kalnay E, Kanamitsu M, Kistler R, Collins W, Deaven D, Gandin L, Iredell M, Saha S, White G, Woollen J (1996) The NCEP/NCAR 40-year reanalysis project. *Bull Am Meteorol Soc* 77:437–471
- King MP, Herceg-Bulic I, Kucharski F, Keenlyside N (2018) Interannual tropical Pacific sea surface temperature anomalies teleconnection to Northern Hemisphere atmosphere in November. *Clim Dyn* 50:1881–1899
- Labat D, Goddérus Y, Probst JL, Guyot JL (2004) Evidence for global runoff increase related to climate warming. *Adv Water Resources* 27:631–642
- Lau KM, Li MT (1984) The monsoon of East Asia and its global associations—a survey. *Bull Amer Meteorol Soc* 65:114–125
- Linkin ME, Nigam S (2008) The north pacific oscillation–West pacific teleconnection pattern: mature-phase structure and winter impacts. *J Clim* 21:1979–1997. <https://doi.org/10.1175/2007JCLI2048.1>
- Liu X, Yanai M (2001) Relationship between the Indian monsoon rainfall and the tropospheric temperature over the Eurasian continent. *Quart J Roy Meteorol Soc* 127:909–937. <https://doi.org/10.1002/qj.49712757311>
- Liu JP, Curry JA, Wang HJ, Song MR, Horton RM (2012) Impact of declining Arctic sea ice on winter snowfall. *Proc Natl Acad Sci USA* 109:4074–4079. <https://doi.org/10.1073/pnas.1114910109>
- Luo X, Wang B (2018) How autumn Eurasian snow anomalies affect east asian winter monsoon: a numerical study. *Clim Dyn* doi. <https://doi.org/10.1007/s00382-018-4138-y>
- Matsueda M (2011) Predictability of Euro-Russian blocking in summer of 2010. *Geophys Res Lett* 38:L06801. <https://doi.org/10.1029/2010GL046557>
- Matsuura K, Willmott CJ (2009) Terrestrial air temperature: 1900–2008 gridded monthly time series (version 4.01), University of Delaware Dept. of Geography Center, Accessed 6 Aug 2015. (Available at http://www.esrl.noaa.gov/psd/data/gridded/data.UDel_AirT_Precip.html)
- Miyazaki C, Yasunari T (2008) Dominant interannual and decadal variability of winter surface air temperature overAsia and the surrounding oceans. *J Clim* 21:1371–1386
- North GR, Moeng FJ, Bell TL, Cahalan RF (1982a) The latitude dependence of the variance of zonally averaged quantities. *Mon Wea Rev* 110:319–326

- North GR, Bell TL, Cahalan RF, Moeng FJ (1982b) Sampling errors in the estimation of empirical orthogonal functions. *Mon Wea Rev* 110:699–706
- Otomi Y, Tachibana Y, Nakamura T (2013) A possible cause of the AO polarity reversal from winter to summer in 2010 and its relationship to hemispheric extreme summer weather. *Clim Dyn* 40:1939–1947
- Park HJ, Ahn JB (2016) Combined effect of the arctic oscillation and the western pacific pattern on East Asia winter temperature. *Clim Dyn* 46:3205–3221
- Rayner NA, Parker DE, Horton EB, Folland CK, Alexander LV, Rowell DP, Kent EC, Kaplan A (2003) Global analyses of sea surface temperature, sea ice, and night marine air temperature since the late nineteenth century. *J Geophys Res* 108:4407
- Smith TM, Reynolds RW, Peterson TC, Lawrimore J (2008) Improvements to NOAA's historical merged land-ocean surface temperature analysis (1880–2006). *J Clim* 21:2283–2296
- Stott PA, Stone DA, Allen MR (2004) Human contribution to the European heatwave of 2003. *Nature* 432:610–614. <https://doi.org/10.1038/nature03089>
- Sun C, Yang S, Li WJ, Zhang R, Wu R (2016) Interannual variations of the dominant modes of East Asian winter monsoon and possible links to arctic sea ice. *Clim Dyn* 47:481–491
- Takaya K, Nakamura H (2001) A formulation of a phase-independent wave-activity flux for stationary and migratory quasigeostrophic eddies on a zonally varying basic flow. *J Atmos Sci* 58:608–627
- Thompson DWJ, Wallace JM (2000) Annular modes in the extra-tropical circulation. Part I: month-to-month variability. *J Clim* 13:1000–1016
- Wallace J, Gutzler D (1981) Teleconnections in the geopotential height field during the Northern Hemisphere winter. *Mon Wea Rev* 109:784–812
- Wang B, Wu Z, Chang CP, Liu J, Li J, Zhou T (2010) Another look at interannual-to-interdecadal variations of the East Asian winter monsoon: the northern and southern temperature modes. *J Clim* 23:1495–1512
- Wu R, Chen S (2016) Regional change in snow water equivalent–surface air temperature relationship over Eurasia during boreal spring. *Clim Dyn* 47:2425–2442
- Wu B, Wang J (2002) Winter arctic oscillation, Siberian high and East Asian winter monsoon. *Geophys Res Lett* 29:1897. <https://doi.org/10.1029/2002GL015373>
- Wu ZW, Wang B, Li J, Jin FF (2009) An empirical seasonal prediction model of the East Asian summer monsoon using ENSO and NAO. *J Geophys Res* 114:D18120. <https://doi.org/10.1029/2009JD011733>
- Wu R, Yang S, Liu S, Sun L, Lian Y, Gao Z (2011) Northeast China summer temperature and North Atlantic SST. *J Geophys Res* 116:D16116. <https://doi.org/10.1029/2011JD015779>
- Wu ZW, Li XX, Li YJ, Li Y (2016) Potential influence of Arctic sea ice to the interannual variations of East Asian spring precipitation. *J Clim* 29:2797–2813
- Yao PZ (1995) The climate features of summer low temperature cold damage in northeast China during recent 40 years. *J Catastrophol* 10:51–56 (in Chinese)
- Yasunari T, Kitoh A, Tokioka T (1991) Local and remote responses to excessive snow mass over Eurasia appearing in the northern spring and summer climate—a study with the MRI GCM. *J Meteor Soc Jpn* 69:473–487
- Ye L, Yang G, Van Ranst E, Tang H (2013) Time-series modeling and prediction of global monthly absolute temperature for environmental decision making. *Adv Atmos Sci* 30:382–396
- Ye K, Wu R, Liu Y (2015) Interdecadal change of Eurasian snow, surface temperature, and atmospheric circulation in the late 1980s. *J Geophys Res* 120:2738–2753. <https://doi.org/10.1002/2015JD023148>

Publisher's Note Springer Nature remains neutral with regard to jurisdictional claims in published maps and institutional affiliations.